

[ATLAS Semivisible Jets]

[Elena Laura Busch]

Submitted in partial fulfillment of the  
requirements for the degree of  
Doctor of Philosophy  
under the Executive Committee  
of the Graduate School of Arts and Sciences

COLUMBIA UNIVERSITY

2024

© 2024

[Elena Laura Busch]

All Rights Reserved

## Abstract

[ATLAS Semivisible Jets]

[Elena Laura Busch]



conclusions reached. Individual chapters should not have abstracts.

## Table of Contents

Acknowledgments . . . . .	v
Dedication . . . . .	vi
Introduction or Preface . . . . .	1
Chapter 1: The Standard Model . . . . .	2
2.1 LHC Timeline . . . . .	4
2.2 Accelerator Physics . . . . .	5
2.2.1 The Journey of a Proton . . . . .	5
2.2.2 Magnets . . . . .	7
2.3 Luminosity . . . . .	7
Chapter 3: The ATLAS Detector . . . . .	10
3.1 Coordinate System and Geometry . . . . .	10
3.2 Inner Detector . . . . .	12
3.2.1 Pixel Detector . . . . .	12
3.2.2 Semiconductor Tracker . . . . .	12
3.2.3 Transition Radiation Tracker . . . . .	13

3.3 Calorimeters . . . . .	13
3.3.1 Liquid Argon Calorimeter . . . . .	13
Conclusion or Epilogue . . . . .	17
References . . . . .	21
Appendix A: Experimental Equipment . . . . .	23
Appendix B: Data Processing . . . . .	24

## List of Figures

2.1	Timeline of LHC activities [9]	5
2.2	The LHC accelerator complex at CERN [11]	6
2.3	The octants of the LHC and location of various beam activities [10]	8
3.1	ATLAS calorimetery system [13]	14
3.2	Diagram of a segment of the EMB, demonstrating the accordion plate arrangement [14]	15
3.3	A LAr pulse as produced in the detector (triangle) and after shaping (curve) [14]	16

## **List of Tables**

## **Acknowledgements**

Insert your acknowledgements text here. This page is optional, you may delete it if not needed.

## **Dedication**

Dedicated to my friends and family

## **Introduction or Preface**

Insert your preface text here if applicable. This page is optional, you may delete it if not needed. If you delete this page make sure to move page counter comment in thesis.tex to correct location.

# Chapter 1: The Standard Model

Four fundamental forces

The Standard Model is a universally accepted framework which explains most of the interactions of fundamental particles. The SM is a renormalizable quantum field theory that obeys the local symmetry  $G_{SM}$ :

$$G_{SM} = SU(3)_C \times SU(2)_L \times U(1)_Y \quad (1.1)$$

The  $SU(3)_C$  symmetry component is the non-Abelian gauge group of quantum chromodynamics (QCD), the theory of strong interactions. There are 8 generators for the  $SU_C(3)$  group which correspond to *gluons*, massless spin-1 gauge boson which carry the force of the strong interaction. Gluon and quarks, the particles which interact with the strong force, carry a color charge  $C$ .

The  $SU(2)_L \times U(1)_Y$  symmetry group represents the electroweak sector of the Standard Model. There are 4 generators for this group, which correspond to the four massless gauge bosons  $W^1$ ,  $W^2$ ,  $W^3$ , and  $B$ . From these massless gauge bosons are formed the massive mediators of the weak force, the  $W^-$ ,  $W^+$  and  $Z^0$  bosons, and the massless electromagnetic force carrier, the photon  $\gamma$ .

The interplay between the fermionic and bosonic fields that emerge from the  $G_{SM}$  symmetry can be described through the Lagrangian in equation 1.2

$$\mathcal{L} = \mathcal{L}_{kin} + \mathcal{L}_\psi + \mathcal{L}_{Yuk} + \mathcal{L}_\phi \quad (1.2)$$

Each term in this Lagrangian describes a set of specific particle physics interactions.  $\mathcal{L}_{kin}$  . with three families of quarks and leptons, and a scalar Higgs doublet. The standard model has 12 gauge bosons: 8 gluons, 3 weak bosons, and the photon. [1]

The physics of the Standard Model of particle physics (SM) is summarized by the SM Lagrangian:

$$\mathcal{L}_{kin} = -\frac{1}{4}F_{\mu\nu}F^{\mu\nu} \quad (1.3)$$

Explain equation

Explain phenomonolyg

## Chapter 2: The Large Hadron Collider

The Large Hadron Collider (LHC) is a 26.7km long circular superconducting high-energy particle accelerator, located approximately 100m underground near the city of Geneva, Switzerland [2]. The LHC occupies the tunnel constructed in 1989 for the Large Electron-Positron (LEP) Collider, and reaches a maximum depth of 170m below the surface. The LHC is operated by the European Organization for Nuclear Research (CERN), the largest international scientific collaboration in the world.

The LHC accelerates protons and heavy ions and collides them at four interaction points around the ring, with a design center-of-mass energy per collision of  $\sqrt{s} = 14$  TeV. Each interaction point is home to one of four detector experiments, which study the products of the collisions. The largest of these experiments is the ATLAS detector, a general purpose detector for studying the Standard Model and searching for physics beyond it [3]. The CMS detector is another general purpose detector, designed and operated independently of the ATLAS detector, but intended to probe the same range of physics [4]. The ALICE experiment is a dedicated heavy ion experiment, and the LHC-b experiment is a dedicated  $b$ -physics experiment [5] [6].

### 2.1 LHC Timeline

The first proton-proton collisions at the LHC were achieved in 2010 at a center-of-mass energy of  $\sqrt{s} = 7$  TeV. Run 1 of the LHC took place between 2010 and 2013. The data collected during this time led to the announcement of the discovery of the Higgs Boson in 2012 [7]. Between 2013 and 2015 the LHC underwent the first Long Shutdown (LS1) during which time key upgrades to the



Figure 2.1: Timeline of LHC activities [9]

physics detectors and the accelerator chain were installed. Run 2 of the LHC was active from 2015 to 2018 and achieved a center-of-mass energy of  $\sqrt{s} = 13$  TeV. Between 2018 and 2022 the LHC underwent the second Long Shutdown (LS2). Run-3 of the LHC began in 2022 and achieved a center-of-mass energy of  $\sqrt{s} = 13.6$  TeV. Run-3 is scheduled to continue through 2026, at which point the LHC machine and detectors will undergo upgrades for the *high luminosity* LHC (HL-LHC), which will increase the number of collisions by a factor of 5-10 with respect to the nominal LHC design [8].

## 2.2 Accelerator Physics

### 2.2.1 The Journey of a Proton

Protons which feed the LHC start as hydrogen gas. The electrons are removed from the hydrogen atoms through the use of strong electric fields. The linear accelerator (LINAC) then accelerates the  $H^-$  ions to an energy of 50 MeV. From here the  $H^-$  ions enter the Proton Synchrotron booster, where they are accelerated up to 1.4 GeV of energy. Subsequently they are sorted into bunches separated in time by 25 ns, where each bunch contains approximately  $10^{11}$  protons. Next the bunches pass through the Proton Synchrotron (PS) and the Super Proton Synchrotron (SPS), where they

## The CERN accelerator complex Complexe des accélérateurs du CERN

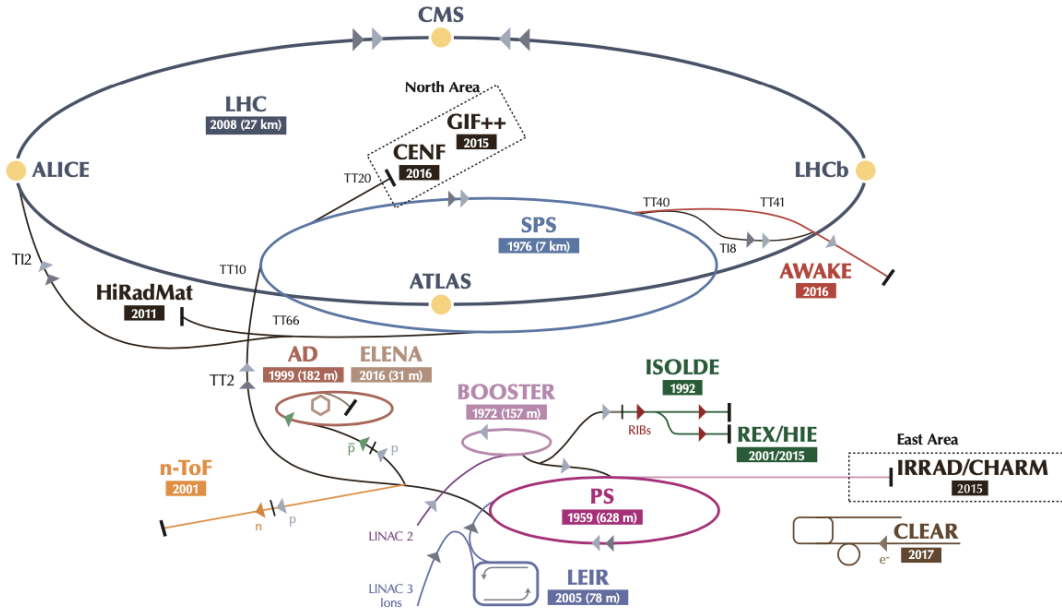


Figure 2.2: The LHC accelerator complex at CERN [11]

reach energies of 25 GeV and 450 GeV respectively. Finally they are injected into the LHC as two beams traveling in opposite direction. The original design allowed each beam to be accelerated up to 7 TeV of energy. Due to limitations with the magnet training, the highest energy actually achieved by the LHC beams during Run 2 was 6.5 TeV each, giving a collision center-of-mass energy of  $\sqrt{s} = 13$  TeV [10]. Figure 2.2 shows the full LHC accelerator complex.

Acceleration in the LHC is performed by eight radio frequency (RF) cavities located around the ring. Each RF cavity produces a 2MV electric field oscillating at 40 MHz. This oscillation is synchronized with the occurrence of the proton bunches produced in the PS. The 40MHz oscillation produces points of stable equilibrium every 2.5ns – a proton bunch occupies this point of A stable equilibrium one out of every ten times, such that the bunches maintain their 25ns spacing [10].

### 2.2.2 Magnets

In addition to the acceleration cavities, the LHC houses 9593 superconducting magnets which direct and focus the proton beam on its 27 kilometer journey. The magnets are comprised of superconducting Niobium-Titanium coils cooled by superfluid helium to 1.9 K. As the beams approach one of the four collision points around the ring, multipole magnets focus and squeeze the beam for optimal collisions [10].

The LHC is divided into sections, where each section contains an a smoothly curving *arc* and a straight *insertion*. The arcs are composed of 1232 large dipole magnets which bend the beam to follow the roughly circular 27 km path. The main dipoles generate powerful 8.3 tesla magnetic fields. Each dipole magnet is 15 meters long and weighs 35 tonnes. The dipoles work in conjunction with quadrupole magnets, which keep the particles in a focused beam, and smaller sextupole, octupole and decapole magnets which tune the magnetic field at the ends of the dipole magnets [12].

The straight insertion sections have different purposes depending on their location around the ring; beam collisions, beam injection, beam dumping, and beam cleaning. At the four collision points, insertion magnets squeeze the beam to ensure a highly focused collision. This is accomplished with a triplet of quadrupole magnets, which tighten the beam from 0.2 millimeters to just 16 micrometers in diameter. Insertion magnets also clean the beam, which prevents stray particles from hitting sensitive components throughout the LHC. When the LHC is ready to dispose of a beam of particles, beam dump magnets deflect the path of the beam into a straight line towards a block of concrete and graphite that stops the beam. A dilution magnet reduces the beam intensity by a factor of 100,000 before the final stop [12].

## 2.3 Luminosity

Collisions at the LHC occur when the two beams of proton bunches cross at one of the four interaction points. The intensity of collisions is described by the instantaneous luminosity, the

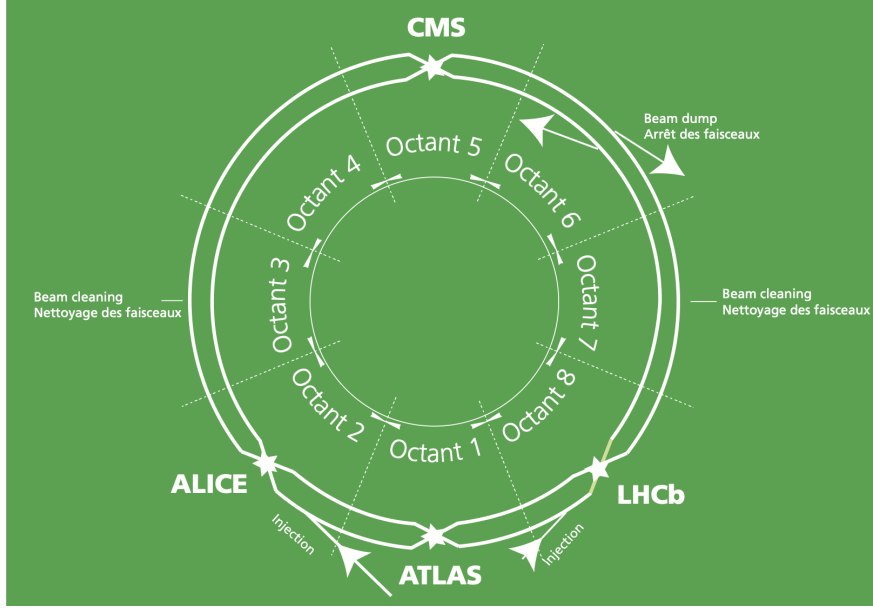


Figure 2.3: The octants of the LHC and location of various beam activities [10]

formula for which is given in equation 2.1. Here  $f$  is the revolution frequency,  $N_1$  and  $N_2$  are the number of particle per bunch for each beam, and  $\sigma_x$ ,  $\sigma_y$  are the horizontal and vertical beam widths. The instantaneous luminosity gives the number of the collisions that could be produced at the interaction point per  $\text{cm}^2$  of cross-sectional area per second.

$$L = \frac{f N_1 N_2}{4\pi \sigma_x \sigma_y} \quad (2.1)$$

The integrated luminosity is obtained by integrating the instantaneous luminosity over time, and measures the total number of collisions which has occurred over the course of running. This is directly correlated with the size of the datasets collected by the LHC experiments.

The design peak luminosity of the LHC is  $1.0 \times 10^{34} \text{ cm}^{-2}\text{s}^{-1}$ . During Run 1 of the LHC the peak instantaneous luminosity achieved was  $0.8 \times 10^{34} \text{ cm}^{-2}\text{s}^{-1}$ . Over the course of Run 1 the LHC collected a total integrated luminosity of  $5.46 \text{ fb}^{-1}$  at  $\sqrt{s} = 7 \text{ TeV}$ , and  $22.8 \text{ fb}^{-1}$  at  $\sqrt{s} = 8 \text{ TeV}$ . Following the first long shutdown and upgrade phase of operations, the LHC achieved a center of mass energy  $\sqrt{s} = 13 \text{ TeV}$  at the beginning of Run 2 in 2015. The LHC was also able to deliver

$2.0 \times 10^{34} \text{ cm}^{-2}\text{s}^{-1}$  peak instantaneous luminosity, double the design value. During LHC Run 2, from 2015-2018, the LHC delivered  $= 156 \text{ fb}^{-1}$  of integrated luminosity for proton-proton collisions. Run 3 of the LHC began in 2022, and is expected to deliver  $250 \text{ fb}^{-1}$  of integrated luminosity to the ATLAS and CMS experiments by 2026.

The goal of physics analyses at the LHC is to find and study events produced by interesting physics processes within the datasets produced by LHC experiments. The cross section  $\sigma$  of a given process indicates the probability of that process occurring given the beam conditions of the LHC. Multiplying the cross section by the integrated luminosity of a dataset gives the expected number of events for that process within the dataset.

$$N_{\text{events}} = \int L(t) dt \times \sigma = (L) \times \sigma \quad (2.2)$$

The cross section for most processes of interest, especially BSM processes, is several orders of magnitude below the total cross section for the LHC. Therefore maximizing the number of events produced in collisions is crucial to increase the likelihood of producing events from processes of interest. For this reason, maximizing instantaneous luminosity is a key factor in accelerator design and operation.

## Chapter 3: The ATLAS Detector

The ATLAS detector is one of two general purpose physics detectors designed to study the products of the proton-proton collisions produced by the LHC. The detectors is composed of a variety of specialized subsystems, designed to fully capture the large array of physics processes produced in the LHC. The apparatus is 25m high, 44m in length, and weighs over 7000 tons. Collisions occur directly in the center of the apparatus, and the cylindrical design of the detector allows a complete 360 view of any physics objects resulting from the collision to be reconstructed.

Two magnet systems provide strong magnetic fields, which bend the trajectory of charged particles as they pass through the magnetic fields; this allows the calculation of the momentum of the particles. A 2T solenoid magnet provides a uniform magnetic field to the inner layers of the detector. Further out, a toroidal magnet system ( TODO: how many toroids?) provides fields strengths of 0.5 to 1T

### 3.1 Coordinate System and Geometry

The ATLAS detector employs a right hand cylindrical coordinate system. The  $z$  axis is aligned with the beam line, and the x-y plane sits perpendicular to the beam line. The origin is centered on the detector, such that the origin corresponds with the interaction point of the two colliding beams. The detector geometry is usually characterized by polar coordinates, where the azimuthal angle  $\phi$  spans the x-y plane. The polar angle  $\theta$  represents the angle away from the beam line, or  $z$  axis.  $\theta = 0$  aligns with the positive  $z$ -axis, and  $\phi = 0$  aligns with the positive x-axis.

The polar coordinate  $\theta$  is generally replaced by the Lorentz invariant quantity *rapidity*  $y$ .

$$y = \frac{1}{2} \ln\left(\frac{E + p_z}{E - p_z}\right) \quad (3.1)$$

This substitution is advantageous because objects in the detector are traveling at highly relativistic speeds. The relativistic speed of objects passing through the ATLAS detector also means that the masses of the particles are generally small compared to their total energy. In the limit of zero mass, the rapidity  $y$  reduces to the *pseudorapidity*  $\eta$ , which can be calculated directly from the polar angle  $\theta$ .

$$\eta = -\ln\left(\frac{\theta}{2}\right) \quad (3.2)$$

Figure ?? depicts the orientation of the coordinate system with respect to the ATLAS detector, while Figure ?? illustrates the relationship between  $\theta$ ,  $\eta$ , and the beamline axis  $z$ . The distance between physics objects in the detector is generally expressed in terms of the solid angle between them  $\Delta R$ .

$$\Delta R = \sqrt{\Delta\phi^2 + \Delta\eta^2} \quad (3.3)$$

Head on proton-proton collisions are more likely to result in objects with a lot of energy in the transverse plane; glancing proton-proton collisions are more likely to result in objects where most of the energy is directed along the  $z$ -axis. Due to the importance of categorizing these objects, as well as the cylindrical design of the ATLAS detector, the detector is generally divided into regions in  $\eta$ . Each subsystem has a “central” or “barrel” region covering low  $|\eta|$ , while the “forward” or “endcap” regions cover  $|\eta|$  up to 4.9. Each of the three main ATLAS subsystems will be discussed in the following sections.

TODO: include figures (subfigure)

## 3.2 Inner Detector

The Inner Detector (ID) is the ATLAS subsystem closest to the interaction point. The primary purpose of the ID is to determine the charge, momentum, and trajectory of charged particles passing through the detector. With this information the ID is also able to precisely determine interaction vertices.

The ID is composed of three sub-detectors; the pixel detector, the semiconductor tracker (SCT) and the transition radiation tracker (TRT). Figure ?? shows the location of these three subsystems with respect to each other and the interaction point.

### 3.2.1 Pixel Detector

The pixel detector is the first detector encountered by particles produced in LHC collisions. The original pixel detector consists of 3 barrel layers of silicon pixels, positioned at 4cm, 11cm and 14cm from the beamline. There are also 4 disks on each side positioned between 11 and 20cm, providing full coverage  $|\eta| < 2.5$ . The layers are comprised of silicon pixels each measuring 50  $\mu\text{m}$  by 300  $\mu\text{m}$ , with 140 million pixels in total. The pixels are organized into modules, which each contain a set of radiation hard readout electronics chips. In 2014, the Insertable B-layer (IBL) was installed, creating a new innermost layer of the pixel detector sitting just 3.3cm from the beamline. The pixels of the IBL measure 50  $\mu\text{m}$  by 250  $\mu\text{m}$ , and cover a pseudo-rapidity range up to  $|\eta| < 3$ . The IBL upgrade enhances the pixel detector's ability to reconstruct secondary vertices associated with short-lived particles such as the b-quark. The improved vertex identification also helped compensate for increasing pile-up in Run 2.

### 3.2.2 Semiconductor Tracker

The SCT provides at least 4 additional measurements of each charged particle. It employs the same silicon technology as the Pixel Detector, but utilizes larger silicon strips which measure

$80\mu\text{m}$  by  $12.4\text{cm}$ . The SCT is composed of 4 barrel layers, located between  $30\text{cm}$  and  $52\text{cm}$  from the beamline, and 9 end-cap layers on each side. The SCT can distinguish tracks that are separated by at least  $200\mu\text{m}$ .

### 3.2.3 Transition Radiation Tracker

The TRT provides an additional 36 hits per particle track. The detector relies on gas filled straw tubes, a technology which is intrinsically radiation hard. The straws which are each  $4\text{mm}$  in diameter and up to  $150\text{cm}$  in length and filled with xenon gas. The detector is composed of about 50000 barrel region straws and 640000 end-cap straws, comprising 420000 electronic readout channels. Each channel provides a drift time measurement with a spatial resolution of  $170\mu\text{m}$  per straw. As charged particles pass through the detector and interact with the xenon, transition radiation is emitted. The use of two different drift time thresholds allows the detector to distinguish between tracking hits and transition radiation hits.

## 3.3 Calorimeters

The ATLAS calorimeter system is responsible for measuring the energy of electromagnetically and hadronically interacting particles passing through the detector. The calorimeters are located just outside the central solenoid magnet, which encloses the inner detectors. The calorimeters also stop most known particles, with the exception of muons and neutrinos, preventing them from traveling to the outermost layers of the detector. The ATLAS calorimetry system is composed of two subsystems - the Liquid Argon (LAr) calorimeter for electromagnetic calorimetry and the Tile calorimeter for hadronic calorimetry. The full calorimetry system is shown in figure 3.1.

### 3.3.1 Liquid Argon Calorimeter

The LAr calorimeter is a sampling calorimeter designed to trigger on and measure the energies of electromagnetic particles, as well as hadronic particles in the high  $\eta$  regions. It is divided in several regions, as shown in Figure 3.1. For the region  $|\eta| < 1.4$ , the electromagnetic barrel (EMB) is

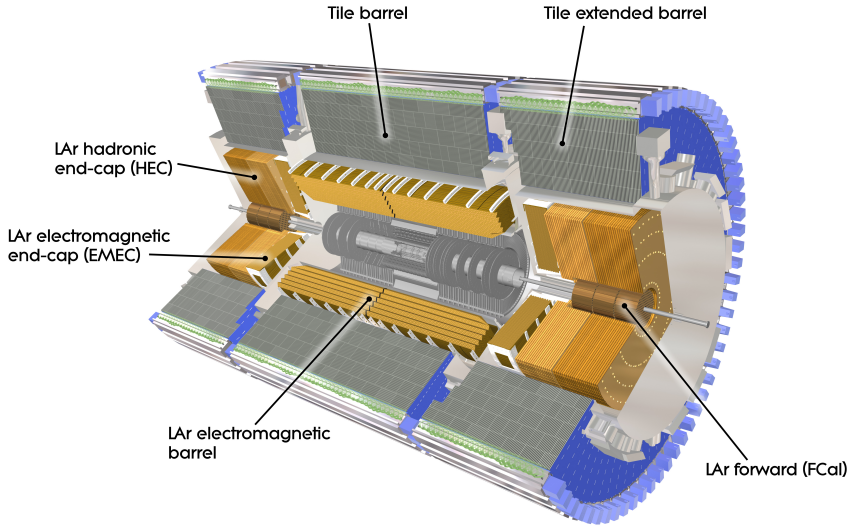


Figure 3.1: ATLAS calorimetery system [13]

responsible for electronic calorimetery, and provides high resolution energy, timing, and position measurements for electrons and photons passing through the detector. The electromagnetic endcap (EMEC) provides additional EM calorimetery up to  $|\eta| < 3.2$ . In the region  $1.4 < |\eta| < 3.2$ , the hadronic endcap (HEC) provides hadronic calorimetery. For hadronic calorimetery In the region  $|\eta| < 1.4$ , corresponding to a detector radii  $> 2.2\text{m}$ , the less expensive tile calorimeter (discussed in the next section) is used instead. A forward calorimeter (FCAL) extends the hadronic calorimetery coverage up to the limit at  $|\eta| = 4.8$  [14].

The LAr calorimeter is composed of liquid argon sandwiched between layers of absorber material and electrodes. Liquid argon is advantageous as a calorimeter active medium due to its natural abundance and low cost, chemical stability, radiation tolerance, and linear response over a large energy range [15]. The calorimeter is cooled to 87k by three cryostats: one barrel cryostat encompassing the EMB, and two endcap cryostats. The barrel cryostat also encloses the solenoid which produces the 2T magnetic field for the inner detector. Front end electronics are housed outside the cryostats and are used to process, store and transfer the calorimeter signals.

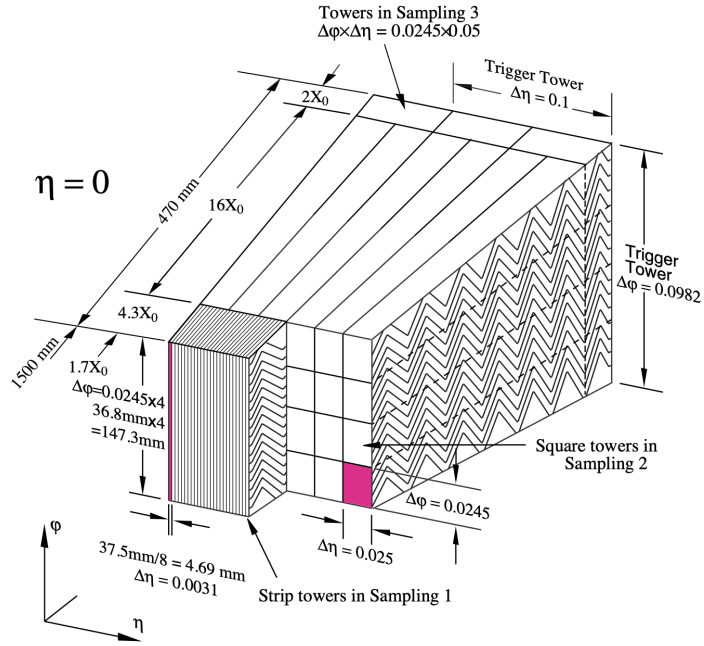


Figure 3.2: Diagram of a segment of the EMB, demonstrating the accordion plate arrangement [14]

For the electromagnetic calorimeter, the layers of electrodes and absorber materials are arranged in an an accordion shape, as illustrated in Figure 3.2. The accordion shape ensures that each half barrel is continuous in the azimuthal angle, which is a key feature for ensuring consistent high resolution measurements. Liquid argon permeates the space between the lead absorber plates, and a multilayer copper-polymide readout board runs through the center of the liquid argon filled gap.

The detection principle for the LAr calorimeter is the current created by electrons which are released when a charged particle ionizes the liquid argon. In the barrel region, the electrons are driven towards the center electrodes by a 2000V potential with a drift time of less than 450ns [16]. In the endcaps the voltage varies as a function of the radius in order to maintain a flat response [14]. The amount of current produced by the ionized electrons is proportional to the energy of the particle creating the signal. Figure ?? shows the shape of the signal produced in the LAr calorimeter, before and after it undergoes shaping during the readout process. The shaping of the pulse enforces

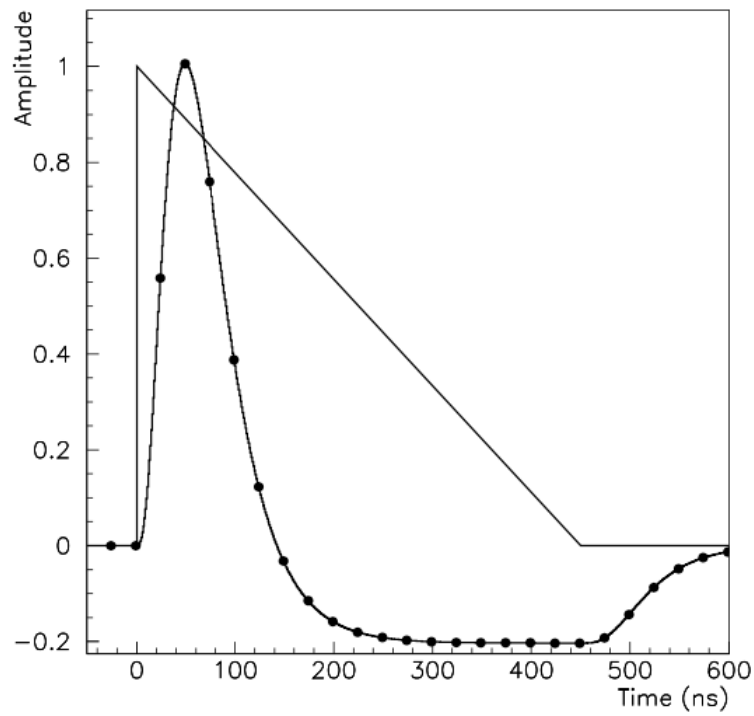


Figure 3.3: A LAr pulse as produced in the detector (triangle) and after shaping (curve) [14]

a positive peak and a negative tail, which ensures that subsequence pulses can be separated with the precision required for the 25ns LHC bunch spacing [14].

## **Conclusion or Epilogue**







## References

- [1] M. Tanabashi et al. “Review of Particle Physics”. In: *Phys. Rev. D* 98 (3 2018), pp. 847–851.
- [2] Lyndon Evans and Philip Bryant. “LHC Machine”. In: *Journal of Instrumentation* 3.08 (2008), S08001.
- [3] “The ATLAS Experiment at the CERN Large Hadron Collider”. In: *JINST* 3 (2008). Also published by CERN Geneva in 2010, S08003.
- [4] “The CMS experiment at the CERN LHC”. In: *Journal of Instrumentation* 3.08 (2008), S08004.
- [5] “The ALICE experiment at the CERN LHC”. In: *Journal of Instrumentation* 3.08 (2008), S08002.
- [6] “The LHCb Detector at the LHC”. In: *Journal of Instrumentation* 3.08 (2008), S08005.
- [7] Aad G., et al. (ATLAS Collaboration and CMS Collaboration). “Combined Measurement of the Higgs Boson Mass in pp Collisions at  $\sqrt(s) = 7$  and 8 TeV with the ATLAS and CMS Experiments”. In: *Phys. Rev. Lett.* 114 (19 2015), p. 191803.
- [8] O. Aberle et al. *High-Luminosity Large Hadron Collider (HL-LHC): Technical design report*. CERN Yellow Reports: Monographs. Geneva: CERN, 2020.
- [9] *The High-Luminosity LHC*. <https://voisins.web.cern.ch/high-luminosity-lhc-hl-lhc>. Accessed: 2024-01-05.
- [10] Ana Lopes and Melissa Loyse Perrey. *FAQ-LHC The guide*. 2022.
- [11] Esma Mobs. “The CERN accelerator complex in 2019. Complexe des accélérateurs du CERN en 2019”. In: (2019). General Photo.
- [12] *Pulling together: Super Conducting electromagnets*. <https://home.cern/science/engineering/pulling-together-superconducting-electromagnets>. Accessed: 2024-01-05.
- [13] Joao Pequenao. *Computer Generated image of the ATLAS calorimeter*. 2008.
- [14] *ATLAS liquid-argon calorimeter: Technical Design Report*. Technical design report. ATLAS. Geneva: CERN, 1996.

- [15] H A Gordon. “Liquid argon calorimetry for the SSC”. In: ().
- [16] Henric Wilkens and (on behalf ofthe ATLAS LArg Collaboration). “The ATLAS Liquid Argon calorimeter: An overview”. In: *Journal of Physics: Conference Series* 160.1 (2009), p. 012043.

## **Appendix A: Experimental Equipment**

  Lorem ipsum dolor sit amet, consectetur adipiscing elit, sed do eiusmod tempor incididunt ut labore et dolore magna aliqua. Ut enim ad minim veniam, quis nostrud exercitation ullamco laboris nisi ut aliquip ex ea commodo consequat. Duis aute irure dolor in reprehenderit in voluptate velit esse cillum dolore eu fugiat nulla pariatur. Excepteur sint occaecat cupidatat non proident, sunt in culpa qui officia deserunt mollit anim id est laborum.

## **Appendix B: Data Processing**

  Lorem ipsum dolor sit amet, consectetur adipiscing elit, sed do eiusmod tempor incididunt ut labore et dolore magna aliqua. Ut enim ad minim veniam, quis nostrud exercitation ullamco laboris nisi ut aliquip ex ea commodo consequat. Duis aute irure dolor in reprehenderit in voluptate velit esse cillum dolore eu fugiat nulla pariatur. Excepteur sint occaecat cupidatat non proident, sunt in culpa qui officia deserunt mollit anim id est laborum.